

# Reconstruction and future prediction of the sea surface from radar observations

A. P. Wijaya<sup>a,b,\*</sup>, P. Naaijen<sup>c</sup>, Andonowati<sup>b,d</sup>, E. van Groesen<sup>a,b</sup>

<sup>a</sup>*Applied Mathematics, University of Twente, Netherlands*

<sup>b</sup>*LabMath-Indonesia, Bandung, Indonesia*

<sup>c</sup>*Maritime & Transport Technology, Technical University Delft, Netherlands*

<sup>d</sup>*Mathematics, Institut Teknologi Bandung, Indonesia*

---

## Abstract

For advanced offshore engineering applications the prediction with available nautical X-band radars of phase-resolved incoming waves is very much desired. At present, such radars are already used to detect averaged characteristics of waves, such as the peak period, significant wave height, wave directions and currents. A deterministic prediction of individual waves in an area near the radar from remotely sensed spatial sea states needs a complete simulation scenario such as will be proposed here and illustrated for synthetic sea states and geometrically shadowed images as synthetic radar images. The slightly adjusted shadowed images are used in a dynamic averaging scenario as assimilation data for the ongoing dynamic simulation that evolves the waves towards the near-radar area where no information from the radar is available.

The dynamic averaging and evolution scenario is rather robust, very efficient and produces qualitatively and quantitatively good results. For study cases of wind waves and multi-modal wind-swell seas, with a radar height of 5 times the significant wave height, the correlation between the simulated and the actual sea is found to be at least 90%; future waves can be predicted up to the physically

---

\*Corresponding author at : LabMath-Indonesia, Jl. Dago Giri no 99, Warung Caringin, Mekarwangi, 40391 Bandung, Indonesia. Tel : +62 22 2507476

Email address: a.parama@labmath-indonesia.org (A. P. Wijaya )

maximal time horizon with an averaged correlation of more than 80%.

*Keywords:* remote sensing, sea surface reconstruction, sea surface prediction, multi-modal sea states, radar image, dynamic averaging.

---

## 1. Introduction

Attempts to use remote sensing of the sea surface for prediction of the actual and future surface elevation in the vicinity of floating ships or offshore structures is motivated by various offshore and maritime engineering applications. Positioning of vessels would benefit from knowledge of the near future incoming low and high waves. Helicopter landing and loading / off-loading operations with at least one floating structure involved are examples of operations of which the critical phase (touch down or lift off) is conducted preferably during a time window with low waves. These workable time windows may occur as well in relatively high seas making their prediction very valuable to increase operational time. Knowing the approach of a freak wave, which seems to occur much more frequently than previously thought, can help to control ships in a safer way (Clauss et al., 2014). An attractive option for the remote wave sensor is the nautical X-band radar. Much attention has been given since several decades to its application as a wave sensor. The vast majority of the efforts so far has been based on spectral 3D FFT methods dedicated to retrieve statistical wave parameters such as mean wave period, wave direction, non-phase-resolved directional wave spectra and properties that could be derived from the surface elevation like water depth and surface current speed and direction. Young et al. (1985) used spectral analysis to detect currents, and Ziemer and Rosenthal (1987) proposed the use of a modulation transfer function to derive surface elevation from radar images of the sea surface. Borge et al. (1999) used the signal-to-noise (SNR) ratio in radar images to propose an approximate relation for the significant wave height with two parameters that have to be calibrated. The question how to

25 reveal the exact relation between radar images and wave elevation / significant  
26 wave height has been subject to many more publications, see e.g. Buckley and  
27 Aler (1998) and Gangeskar (2014). We will not address this topic here, but refer  
28 to a forthcoming publication of Wijaya and van Groesen (2015) that derives the  
29 significant wave height from the shadowed images without any calibration. In  
30 this paper it is assumed that the significant wave height is known, either from  
31 existing analysis techniques of radar images or by means of a reference observa-  
32 tion such as a wave buoy or recorded ship motions.

33 Some of the rare attempts to retrieve the actual deterministic, i.e. phase re-  
34 solved, wave surface elevation from radar-like images are reported by Blondel  
35 and Naaijen (2012) and Naaijen and Blondel (2012), but the quality was shown  
36 to be not optimal. A very different method has been explored by Aragh and  
37 Nwogu (2008); they use a 4D Var assimilation method, assimilating (raw) radar  
38 data in an evolving simulation. Nevertheless, it seems that in literature no sta-  
39 tistically significant evidence has been reported for successful deterministic wave  
40 sensing (reconstruction), nor any method to propagate the waves to a blind area  
41 or to provide predictions.

42 To overcome the 'blind' zone around the radar where no elevation information is  
43 available, a propagation model is needed to evolve phase resolved reconstructed  
44 waves in the visible area into the blind zone and to make future predictions of  
45 the waves there, e.g. at the position of the ship carrying the radar antenna.

46 The main aim of this paper is to present a scenario that integrates the inversion  
47 of the observed images with the propagation and prediction. This integration  
48 is achieved by a robust dynamic averaging-evolution procedure which will be  
49 shown to provide a prediction accuracy that is significantly higher than the ac-  
50 curacy of the observation of a single image itself.

51 In the following we will restrict to the case that the radar position is fixed; im-

52 ages from a radar on a ship moving towards the waves will require some obvious  
 53 adaptations, and will reduce the prediction horizon. The complete evolution sce-  
 54 nario takes into account the specific geometry determined by the radar scanning  
 55 characteristics. For the common nautical X-band radars one can distinguish the  
 56 ring-shaped area where information from radar scans is available, and the near  
 57 radar area where this information is missing. Through the outer boundary of  
 58 the ring, some 2000 m away from the radar, waves enter and leave the area;  
 59 part of the incoming waves evolve towards the near-radar area or interact with  
 60 waves that determine the elevation there. Hence, updates to catch the incoming  
 61 waves have to be used repeatedly. The inner boundary of the ring determines  
 62 the disk, the near-antenna area with a radius of some 500 m; there no useful  
 63 radar information is available because the backscatter is too high and/or suf-  
 64 fers from interaction effects with the ship's hull. A propagation model has to  
 65 evolve the information from the ring area inwards to the radar position. This  
 66 description defines the main ingredients of a process that has to be developed  
 67 into a practical scenario that is sufficiently efficient and accurate, noting that  
 68 the quality of the simulated elevation in the near-radar area depends on the  
 69 quality of the simulation in the radar ring. Since radar images give only par-  
 70 tial and distorted information about the actual sea surface, mainly because of  
 71 the shadowing effect, a phase resolved reconstruction of the sea - the inversion  
 72 problem - is important. As we will show, the use of a sequence of images in a  
 73 spatially dynamic scenario will predict the present and future sea surface in a  
 74 reasonable degree of accuracy.

75 We start to propose two simple reconstruction methods for single images, but  
 76 fail to reduce the effects of shadowing noticeably; consecutive simulations with  
 77 the raw and the the reconstructed images will provide an indication of the ro-  
 78 bustness of the complete scenario. Indeed, the quality of the reconstruction will

79 be substantially enhanced by the dynamic averaging and evolution procedure,  
 80 almost independent of the choice of these initial images. The procedure consists  
 81 of the averaging of a few successive (reconstructed) images, together with the  
 82 result of the dynamic simulation, to produce updates that are assimilated in the  
 83 dynamic simulation. We will use the full ring shaped observation domain sur-  
 84 rounding the target location; this makes it possible to reconstruct and predict  
 85 uni-modal wind waves as well as multi-modal seas with wind waves and swell(s)  
 86 coming from possibly substantially different directions. Specific attention will  
 87 be paid to the question how to treat the evolution of multi-modal seas in the  
 88 proposed scenario.

89 In this paper we use synthetic data and make some simplifications for ease of  
 90 presentation, but the scenario to be described can also be applied for more real-  
 91 istic cases. The use of synthetic data makes it possible to quantify the quality of  
 92 the results which will be difficult to achieve in field situations for which reliable  
 93 data of the surface elevation both in the ring-shaped observation area and the  
 94 near-radar area simultaneously are very difficult to obtain. The wind and wind-  
 95 swell seas that we synthesize are chosen to be linear to simplify the evolution,  
 96 but linearity is not essential. From the synthetic seas, we construct synthetic  
 97 radar images by only taking the geometric effect of shadowing into account as  
 98 an illustration that the scenario can resolve imperfections of that kind.

99 The paper is arranged according to the successive steps in the proposed sce-  
 100 nario. Section 2 will describe the design of (multi-modal) synthetic seas and  
 101 of synthetic radar images by applying the shadowing effects. In Section 3 the  
 102 complete dynamic averaging-evolution scenario (DAES) will be described to de-  
 103 termine from the shadowed images the wave elevation inside the observable area  
 104 and inside the blind area near the radar. Section 4 describes the results for two  
 105 case studies, one case of wind waves, and the other one for wind-swell seas;

106 apart from reconstruction results, the quality of predictions are investigated up  
107 to the maximal prediction time. In section 5 the results of the study case are  
108 discussed and conclusive remarks will be given in section 6.

## 109 **2. Synthetic data**

110 After a motivation to restrict the investigations to shadowed seas in the first  
111 subsection, we describe the construction of the synthetic surface elevation maps.  
112 These will be used in subsection 2.3 to generate the synthetic geometric images  
113 that take into account the shadowing effect, and later to quantify the quality of  
114 the reconstructed and evolved surface elevations.

### 115 *2.1. Simplifications*

116 When the sea will be scanned by the radar, parts of it will be hidden for the  
117 electromagnetic radar waves since they are partly blocked by waves closer to  
118 the radar, the geometric shadowing. It should be remarked that investigations  
119 of radar data by Plant and Farquharson (2012a) do not support the hypothesis  
120 that geometric shadowing plays a significant role at low-grazing-angle; indica-  
121 tions are found that shadowing rather occurs as so-called partial shadowing.  
122 Besides shadowing, tilt (slope of the sea surface relative to the look-direction of  
123 the radar) is considered to be an important modulation mechanism for wave ob-  
124 servations by radar, see Borge et al. (2004) and Dankert and Rosenthal (2004).  
125 In all these references the so-called hydrodynamic modulation as described by  
126 e.g. Alpers et al. (1981) has been ignored. Possible other effects perturbing  
127 the observation that are introduced by specific hardware related properties of  
128 a radar system should in general be invertible when the exact properties are  
129 known, which is why we do not consider that aspect here.

130 In this paper we will consider as example of imperfections of the observed sea  
131 the effect of geometric shadowing. For this relevant effect it will be shown how

well the proposed averaging-evolution scenario can cope with imperfections with a length scale of the order of one wavelength, virtually independent of the precise cause of the imperfections. Since this geometrical approach is mainly valid as a first order approach of the backscattering mechanism for grazing incidence conditions at far range for marine radar (Borge et al., 2004), electromagnetic diffraction (Plant and Farquharson, 2012b) is not taken into account in this paper. It must be noted that perturbations over larger areas as caused by severe wind bursts may not be recovered accurately by the present methods.

## 2.2. Synthetic surface elevations

To synthesize a sea, we use a linear superposition of  $N$  regular wave components each having a distinct frequency and propagation direction. The wave spectrum  $S_\eta(\omega)$  is defined on an equally spaced discrete set of frequencies  $\omega_n$  covering the significant energy contributions. In order to assure that the sea is ergodic (Jefferys, 1987), it is required that only a single direction corresponds to each frequency. A propagation direction is assigned to each wave component by randomly drawing from the directional spreading function which is used as a probability density function, as proposed by Goda (2010). The directional spreading function with exponent  $s$  around the main direction  $\theta_{main}$  is given by

$$D(\theta) = \begin{cases} \beta \cos^{2s}(\theta - \theta_{main}), & \text{for } |\theta - \theta_{main}| < \pi/2, \\ 0, & \text{else} \end{cases} \quad (1)$$

with normalization  $\beta$  such that  $\int D(\theta) d\theta = 1$ .

With  $k_n$  the length of the wave vectors corresponding to the frequencies  $\omega_n$ , and with  $\phi_n$  phases that are randomly chosen with uniform distribution in

153  $[-\pi, \pi]$ , the sea is then given by

$$\eta(\mathbf{x}, t) = \sum_n \sqrt{2S_\eta(\omega_n)} d\omega \cos(k_n(x \cos(\theta_n) + y \sin(\theta_n)) - \omega_n t + \phi_n) \quad (2)$$

154 Snapshots of the surface elevation at multiples of the radar rotation time  $dt$  are  
 155 given by  $\eta(\mathbf{x}, n \cdot dt)$ .

### 156 2.3. Geometric images

157 With 'Geometric Images' we refer to the synthesized radar observation of  
 158 the surface elevation for which, as stated above, we will only take the geometric  
 159 shadowing into account. Shadowing along rays has been described by Borge et  
 160 al. (2004) and is briefly summarized as follows.

161 After interpolating the image on a polar grid, with the radar at the origin  
 162  $\mathbf{x} = (0, 0)$ , we take a ray in a specific direction, starting at the radar position  
 163 towards the outer boundary, using  $r$  to indicate the distance from the radar.  
 164 We write  $s(r)$  for the elevation along the ray, and  $h_R$  for the height of the  
 165 radar. The straight line to the radar from a point  $(r, s(r))$  at the sea surface  
 166 at position  $r$  is given for  $\rho < r$  by  $z = \ell(\rho, r) = s(r) + a(r - \rho)$  with  $a =$   
 167  $(H_r - s(r)) / r$ . The point  $(r, s(r))$  at the sea surface is visible if  $\ell(\rho, r) > s(\rho)$   
 168 for all  $\rho < r$ , i.e. if  $\min_\rho (\ell(\rho, r) - s(\rho)) > 0$ . At the boundary of such intervals  
 169 the value is zero, and so the visible and invisible intervals are characterized  
 170 by  $\text{sign}[\min_\rho (\ell(\rho, r) - s(\rho))] = 0$  and  $= -1$  respectively. This leads to the  
 171 definition of the characteristic visibility function as

$$\chi(r) = 1 + \text{sign} \left[ \min_\rho \{ \Theta(r - \rho) \Theta(\rho) (\ell(\rho, r) - s(\rho)) \} \right] \quad (3)$$

172 where  $\Theta$  is the Heaviside function, equal to one for positive arguments and zero  
 173 for negative arguments. The visibility function equals 0 and 1 in invisible and  
 174 visible intervals respectively. The shadowed wave ray, as seen by the radar, is



175 then given by

$$s_{shad}(r) = s(r) \cdot \chi(r) \quad (4)$$

176 which defines the spatial shadow operator along the chosen ray. Repeating this  
177 process on rays through the radar for each direction, leads to the shadowed sea,  
178  $S_{shad}(\mathbf{x})$ .

179 The geometric image is obtained by removing information in a circular area  
180 around the radar position with a radius of  $r_0$ . Then the geometric image is  
181 described by

$$I(\mathbf{x}) = S_{shad}(\mathbf{x}) \cdot \Theta(|\mathbf{x}| - r_0) \quad (5)$$

### 182 **3. Dynamic averaging-evolution scenario**

183 This section presents the dynamic averaging-evolution scenario (DAES) that  
184 will provide a reconstruction and prediction of the surface elevation at the radar  
185 position using the geometrically shadowed waves in the ring-shaped observation  
186 area of the sea. The main ideas can be described as follows.

187 The exact (non-shadowed) sea is supposed to evolve according to a linear (dis-  
188 persive) evolution operator. Except from entrance effects of waves through the  
189 boundary, one snapshot of the sea would be enough to determine exactly the  
190 whole future evolution. The effects of shadowing give a space and time depen-  
191 dent perturbation for all images: the amount of shadowing (visibility) depends  
192 on the distance from the radar, and the position in time of the waves deter-  
193 mines the actual area of shadowing, shifting and changing somewhat with the  
194 progression of the wave. Hence, one snapshot of the observed (shadowed) sea,  
195 will produce a different evolution result than that of the exact sea because the  
196 zero-level of the shadowed area will be evolved. In order to control, and actually  
197 reduce, the error, we use updates to be assimilated in the dispersive evolution.  
198 After three radar rotation times  $3dt$  we update the ongoing simulation by assim-

199 ilation with the averaged 3 preceding images, where the averaging itself already  
200 reduces the effect of shadowing somewhat. Since we do this globally, so also in  
201 areas closer to the radar where the shadowing is less severe, the result with the  
202 dynamic averaging-evolution scenario shows that this is sufficiently successful  
203 to give an acceptable correlation in the radar area.

204 The first subsection deals with two simple methods that aim to improve the  
205 quality of each individual geometric image by attempting to fill in the gaps  
206 caused by the shadowing. Then the evolution of a single image is discussed in  
207 some detail, after which the dynamic averaging of several images is described  
208 to construct updates that will be used in subsection four as assimilation data  
209 in an evolution of the full sea.

### 210 *3.1. Spatial reconstruction of geometric images*

211 In the following, two methods will be presented for a first attempt to recon-  
212 struct the geometric images in regions where the observation is shadowed.

213 In the first method the geometric image is shifted vertically such that the spatial  
214 average (over the observation area) vanishes. With a scaling factor  $\alpha$  to obtain  
215 the correct significant wave height, this will produce the reconstructions  $R_n^1$  as

$$R_n^1(\mathbf{x}) = \alpha (I_n(\mathbf{x}) - \text{mean}(I_n)) \quad (6)$$

216 As mentioned in the introduction, it is assumed that the true variance of the  
217 waves (or significant wave height) is known from either additional analysis  
218 and/or a reference measurement so that  $\alpha$  is determined.

219 The second proposed method is described as

$$R_n^2(\mathbf{x}) = \alpha (I_n(\mathbf{x}) - E(I_n, -T/2)) \quad (7)$$

Here  $E(I_n, -T/2)$  evolves the sea backwards in time over half of the peak period, for which in multi-modal seas we will take the peak period of the wind waves. The evolution indicated here with the operator  $E$  will be explained in detail in the next subsection. Note that for harmonic long crested waves with period  $T$  of which negative elevations have been put to zero elevation (to roughly resemble the effect of shadowing) leads to the correct harmonic wave by the reconstruction  $R^2$ .

### 3.2. Evolution of a single image

Let the reconstructed geometric image, denoted by  $R$ , obtained by either reconstruction method described in the previous subsection, be given by its 2D Fourier description as:

$$R(\mathbf{x}) = \sum_{\mathbf{k}} a(\mathbf{k}) e^{i\mathbf{k} \cdot \mathbf{x}} \quad (8)$$

Here  $\mathbf{k}$  is the 2D wave vector, and the coefficients  $a$  can be obtained by applying a 2D FFT on  $R$ .

The image itself is not enough to define the evolution uniquely since the information in which direction the components progress with increasing time is missing. For given direction vector  $\mathbf{e}$ , define the forward evolution as

$$E_{\mathbf{e}}(R, t) = \sum_{\mathbf{k}} a(\mathbf{k}) \exp i [\mathbf{k} \cdot \mathbf{x} - \text{sign}(\mathbf{k} \cdot \mathbf{e}) \Omega(k) t] \quad (9)$$

where  $k = |\mathbf{k}|$  and  $\Omega(k) = \sqrt{gk \tanh(kD)}$  is the exact dispersion above depth  $D$ . Waves propagating in a direction  $\tilde{\mathbf{e}}$  that makes a positive angle with  $\mathbf{e}$ , so  $\tilde{\mathbf{e}} \cdot \mathbf{e} > 0$ , will then propagate in the correct direction for increasing time, which justifies to call the evolution forward propagating with respect to  $\mathbf{e}$ . Changing the minus-sign into a plus-sign in the phase factor, the backward propagating evolution in the direction  $-\mathbf{e}$  is obtained.

For uni-modal sea states, such as wind waves or swell, there will be a main

243 propagation direction  $\mathbf{e}_{prop}$ , which is the direction of propagation of the most  
 244 energetic waves. Other waves in such wave fields will usually propagate in nearby  
 245 directions, under an angle less than  $\pi/2$  different from the main direction. In  
 246 such cases we can take  $\mathbf{e}_{prop}$  as the direction to define the evolution. Actually,  
 247 any direction from the dual cone of wave vectors can be chosen, i.e. any vector  
 248 that has positive inner product with all wave directions.

249 In multi-modal sea states, in most practical cases a combination of wind waves  
 250 and swell, the situation is different since the waves may have a wider spreading  
 251 than the  $\pi/2$  difference from the main direction that was assumed for the uni-  
 252 modal sea states. When the wave directions are spread out over more than a  
 253 half space, one evolution direction so that all waves are propagated correctly  
 254 cannot be found anymore. If only low-energy waves are outside a half space,  
 255 one may still use a forward propagating evolution operator. Then an optimal  
 256 choice is the main evolution direction for which the maximum portion of the  
 257 total wave energy is evolved correctly. A way to identify this optimal direction  
 258 is discussed now.

259 Practically, we use a second (or more) 'control' image, and look for which vector  
 260  $\mathbf{e}$  the evolution of the first image corresponds with the control image as good as  
 261 possible in least-square norm; this then determines the *main evolution direction*  
 262 (MED). Explicitly, given two successive images of the wave field, say  $R_1$  and  $R_2$   
 263 a small time (the radar rotation time)  $dt$  apart, we compare  $R_2$  with the forward  
 264 evolution of  $R_1$  over time  $dt$  in the direction  $\mathbf{e}$ , to be denoted by  $E_{\mathbf{e}}(R_1)$ , and  
 265 minimize the difference over all directions  $\mathbf{e}$ , defining the MED as the optimal  
 266 value

$$\mathbf{e}_{MED} \in \min_{\mathbf{e}} |E_{\mathbf{e}}(R_1) - R_2|. \quad (10)$$

267 Instead of minimizing a norm of the difference, one can also take the maximum  
 268 of the correlation. For fields with limited directional spreading there will be a

269 broad interval of optimal directions, in which case the average of the optimal  
 270 directions can be chosen. For cases of multi-modal sea states where the main  
 271 propagation direction of the different modes deviate very much there is likely  
 272 to be one distinct optimal MED. It is possible that with this method using the  
 273 MED, a significant amount of wave energy is evolved in the wrong direction,  
 274 depending on how much the main directions of the different modes differ.  
 275 In the following we will use a simplified notation when evolving over one time  
 276 step  $dt$ , namely

$$\mathcal{E}(R) = E_{\mathbf{e}_{MED}}(R, dt) \quad (11)$$

277 Evolving over several time steps, say  $m.dt$ , is then written as a power (succession  
 278 of evolution)  $\mathcal{E}^m$ .

### 279 *3.3. Updates from dynamic averaging*

280 The reconstruction process described in subsection 3.1 gives approximate sea  
 281 states  $R_n$ . The study cases will show that these reconstructions are still rather  
 282 poor when compared to the exact synthetic surface elevation maps; the corre-  
 283 lation with the exact surface is only slightly better than that for the shadowed  
 284 geometric images. In order to reduce the effect of this reconstruction error and  
 285 thereby to improve the accuracy of the elevation prediction near the radar, we  
 286 propose an averaging procedure in physical space. This procedure will involve  
 287 three successive reconstructed images and the simulated wave field at the in-  
 288 stant of the last image.

289 To set notation, the simulated sea (the simulation process will be detailed  
 290 below) at time  $t$  will be denoted as  $\zeta(\mathbf{x}, t)$ ; at discrete times  $m.dt$  we write  
 291  $\zeta_m(\mathbf{x}) = \zeta(\mathbf{x}, m.dt)$ .

292 The simulation is initialized by taking for the first three time steps the three

293 successive reconstructed images

$$\zeta_m(\mathbf{x}) = R_m(\mathbf{x}) \text{ for } m = 1, 2, 3$$

294 For the continuation, updates will be used to assimilate the evolution. We  
 295 describe the update process at a certain time  $t_0$ , which is a multiple of  $3dt$ .  
 296 Available at that time are the simulated wave field at  $t_0$ , to be denoted by  
 297  $\zeta_0(\mathbf{x}) = \zeta(\mathbf{x}, t_0)$ , the reconstructed image at time  $t_0$ , and 2 previous images at  
 298 times  $t_{-1} = t_0 - dt$ ,  $t_{-2} = t_0 - 2dt$ ; these reconstructed images will be denoted by  
 299  $R_{0,-1,-2}$  respectively. Since the images  $R_k$  have substantial inaccuracies despite  
 300 the reconstruction, it can be expected that an averaging procedure improves  
 301 the quality. This averaging has to be done in a dynamic way to compensate for  
 302 the fact that the images are available at different instants in time. Therefore  
 303 the images  $R_{-1}$  and  $R_{-2}$  have to be evolved over one, respectively two, time  
 304 steps  $dt$ . This produces  $\mathcal{E}(R_{-1})$  and  $\mathcal{E}^2(R_{-2})$ , each representing, just as  $R_0$ ,  
 305 an approximation of the sea state at time  $t_0$ . But the information will be  
 306 different, partly complementary, because the information at different time steps  
 307 shows somewhat different parts of the wave because of the shadowing effect.  
 308 Therefore an arithmetic mean will contain more information, and may also  
 309 reduce incidental errors and noise. The ongoing simulation  $\zeta_0$  also gives an  
 310 approximation of the sea at  $t_0$ , and, most important, will also contain elevation  
 311 information in the near-radar area where the  $R_k$  are vanishing. Choosing some  
 312 weight factors, we therefore take as update at time  $t_0$  the following combination

$$U_0(\mathbf{x}) = \left( \frac{1}{6}(R_0 + \mathcal{E}(R_{-1}) + \mathcal{E}^2(R_{-2})) + \frac{1}{2}\zeta_0 \right) (1 - \chi_{rad}) + \zeta_0 \chi_{rad} \quad (12)$$

313 Here  $\chi_{rad}(\mathbf{x})$  is the characteristic function (or a smoothed version) of the near-  
 314 radar area:  $\chi_{rad} = 1$  in the near radar zone where no waves can be observed

315 and  $\chi_{rad} = 0$  in the remaining area. The number of reconstructed images to  
 316 be taken in the update can be more or less than 3, and each could be given a  
 317 different weight. Our experience with various test cases led to the weight factors  
 318 as taken above.

### 319 3.4. Evolution and prediction

320 The updates defined above will be used as assimilation data to continue the  
 321 simulation. In detail, after the construction of an update, say  $U_{3m}$ , the simula-  
 322 tion continues with this sea state as initial elevation field for three consecutive  
 323 time steps:

$$\zeta_{3m+j} = \mathcal{E}^j(U_{3m}) \text{ for } j = 1, 2, 3. \quad (13)$$

324 This defines the full evolution in time steps  $dt$ , which is repeatedly fed with new  
 325 information from the reconstructed images through the updates. This scenario  
 326 can run in real time in pace with incoming real radar images.

327 A prediction can be defined, starting at any time  $t_0 = m \cdot dt$  for a certain time  
 328 interval ahead, without using any information of geometric images later than  
 329  $t_0$ . The prediction, say for a future time of  $\tau \in [0, \Pi]$ , where  $\Pi$  is the prediction  
 330 horizon, is then defined as

$$P(t_0, \tau) = E(\zeta(t_0), \tau) \text{ for } \tau \in [0, \Pi]. \quad (14)$$

331 An upper bound for the prediction horizon depends on the speed of the waves  
 332 and the distance of the outer boundary to the radar. As shown by Wu (2004)  
 333 and Naaijen et al. (2014) the prediction horizon is mainly governed by the  
 334 group velocity of the waves and the size of the observation domain. In case of  
 335 a nautical radar, the spatial observation domain will be the ring-shaped area,  
 336 previously indicated by  $\chi_{rad} = 0$ . The group velocity will be different and in  
 337 different directions for short-crested, in particular multi-modal, seas and depend

on wave characteristics (roughly the peak period) and the depth. These factors will influence the prediction horizon in which we can expect a reliable prediction. Besides that, the prediction horizon  $\Pi$  clearly also depends on the accuracy that is desired for the prediction.

#### 4. Case studies

In this section we present the results for two study cases: one for wind waves and one with combined wind waves and swell. Comparisons are presented between the predicted wave elevation, obtained by processing the synthesized images with the proposed DAES method and the exact wave elevation as it was synthesized. We start to specify the sea data and other physically and numerically relevant parameters of the simulations, followed by the simulation results.

##### 4.1. Parameters of the study cases

###### 4.1.1. Geometry and spatial grid parameters

The seas that we consider evolve above a depth  $h = 50$  m. The height of the radar is an important quantity because the severity of the shadowing effect is governed by the ratio of radar height and wave height. We will report on a value of the radar height  $h_R$  of 15 m above the still water level. The radar is assumed to be at a fixed position above the still water level, with a constant radar rotation speed  $dt = 2$  s. The sea is constructed in an area  $[-2050, 2050]^2$  with a number of nodes in  $x$  and  $y$ -direction equal to  $N_x = N_y = 512$ , so spatial step size  $dx = dy = 7.9$  m. Modeling the outer boundary of the radar observation area, the elevation of each snapshot of the sea is made to vanish for distances from the radar larger than  $r_{max} = 1800$  m. The shadowing procedure is applied after transforming each sea state to polar coordinates  $(r, \phi)$  on a grid with  $dr = 7.5$  m and  $d\phi = 0.3^\circ$ . The geometric image is then obtained by



transforming back to Cartesian coordinates and make the elevation vanish in the circular near radar area of radius  $r_{min} = 500$  m.

#### 4.1.2. Sea states

We provide the properties of the wind waves and the swell separately; since we consider linear waves, the characteristics of the multi-modal sea state, which is a combination of the wind waves and swell, can be derived in a straightforward way. The properties of the waves, with related wave characteristics above depth  $h = 50$  m, are summarized in Table 1.

Table 1: Characteristic of sea and swell waves

Sea	$H_s$	$T_p$	$\gamma$	$\theta_{main}$	$s$	$\omega_p$	$k_p$	$\lambda_p$	$C_p$	$V_g$
Wind	3	9	3	$-\pi/2$	10	0.7	0.05	125	13.9	7.4
Swell	1	16	9	$3\pi/4$	50	0.4	0.02	308	19.2	14.8

The wind waves have main propagation direction from North to South,  $\theta^W = -\pi/2$ ; the wave spreading is given by the spreading function (1) with exponent  $s = 10$ .

The frequency spectrum of the wind waves is a Jonswap spectrum with  $\gamma = 3$ , peak period  $T_p = 9$  s, and significant wave height  $H_s^W = 3$  m. Note that the significant wave height is an important factor that affects the amount of shadowing; the ratio of radar height and significant wave height is as low as 5 in this study case, leading to substantial shadowing.

The multi-modal sea consists of the above wind waves to which is added the swell waves. The swell consists of waves from the South-Eastern direction,  $\theta^S = 3\pi/4$ , peak enhancement factor  $\gamma = 9$ , wave spreading with  $s = 50$ , peak period  $T_p = 16$  s, and significant wave height  $H_s^S = 1$  m. The significant wave height of this combined sea state will be  $H_s^{WS} = \sqrt{10} \approx 3.15$  m, so that the ratio of radar height and significant wave height is slightly less than 5.

The study cases of wind waves without swell and combined wind waves-swell will

387 be denoted by W15 and WS15 respectively. The number of discrete components  
388  $N$  used to synthesize the waves as in equation (2), has been taken  $N = 1500$   
389 for the wind waves and  $N = 700$  for the swell in study case WS15.

#### 390 4.1.3. Main evolution direction

391 As described in subsection 3.2, the main evolution direction MED will be  
392 determined as the direction for which the error of the difference between a one-  
393 step evolved image and the successive image is as small as possible. For the  
394 study cases Figure 1 shows the averaged relative error obtained by comparing  
395 10 pairs of successive reconstruction images for case W15 and WS15. Here, the  
396 angle is measured from the positive  $x$ -axis in counter clockwise direction. For  
397 study case W15 the relative error is rather constant in the interval  $[-150^\circ, -30^\circ]$ ,  
398 with  $-90^\circ$  in the middle of the interval. Hence this is chosen as MED, which  
399 coincides with the design value of the main wind direction of the synthesized  
400 wave field. For case WS15 the situation is very different. There is now only a  
401 small interval of angles identifying evolution directions for which most energy  
402 is propagated correctly. Hence, for case WS15 the angle of minimal error is  
403 chosen as MED, i.e.  $-148^\circ$ . For the study cases using the shadowed images  
404 to determine MED we observed a few degrees difference with the MED's found  
405 when using the synthetic non-shadowed seas; in the following we take the values  
406 obtained from the shadowed seas.

#### 407 4.2. Simulation Results

408 In this paragraph results of the simulations will be described. After some  
409 graphical presentations, more quantitative information is presented for the re-  
410 construction sea states and the future prediction.

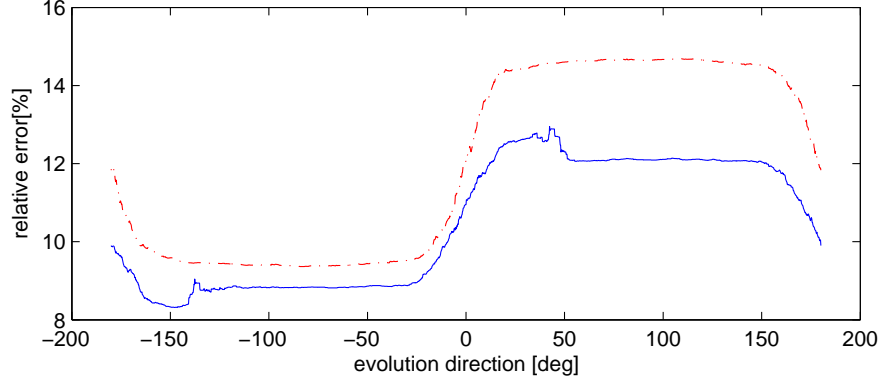


Figure 1: The relative error in the procedure to determine the main evolution direction MED averaged over 10 realizations, for case W15 (dash-dotted red) and WS15 (solid blue).

#### 4.2.1. Graphical presentation

We start with some results that illustrate the DAES method. After the first three synthesized geometric images, the dynamic averaging - evolution scenario is initiated using updates at every time that is a multiple of  $3dt$ . For a certain  $t = t_0$ , shortly after starting the simulation, various images are presented in Figure 2. Figure 2a shows the true wave elevation as synthesized at  $t = t_0$ . Figure 2b shows the shadowed image of the wave elevation depicted in Figure 2a with vanishing elevation in the blind area  $r < 500$  around the antenna. Figure 2c, shows the reconstruction  $U_0(t_0)$  (also denoted by  $P(t_0; \tau = 0)$ ). As can be seen, the wind waves propagating in the main direction from North to South in the negative  $y$ -direction, and more so the swell from SE to NW, have evolved already some small distance into the near-antenna zone. Figure 2d shows the reconstruction  $P(t_1; \tau = 0)$  for a larger value  $t_1$  at which the waves have evolved so much that they occupy the entire blind area near the antenna  $r < 500$ . Figure 3 shows the cross section in the  $y$  direction at  $x = 0$  of the shadowed waves in Figure 2b. Different from Figure 2b, the waves are shown here for  $r < r_{min}$  as well. As can be observed for this particular wave condition and quotient of radar altitude and significant wave height of  $15/3$ , the shadowing

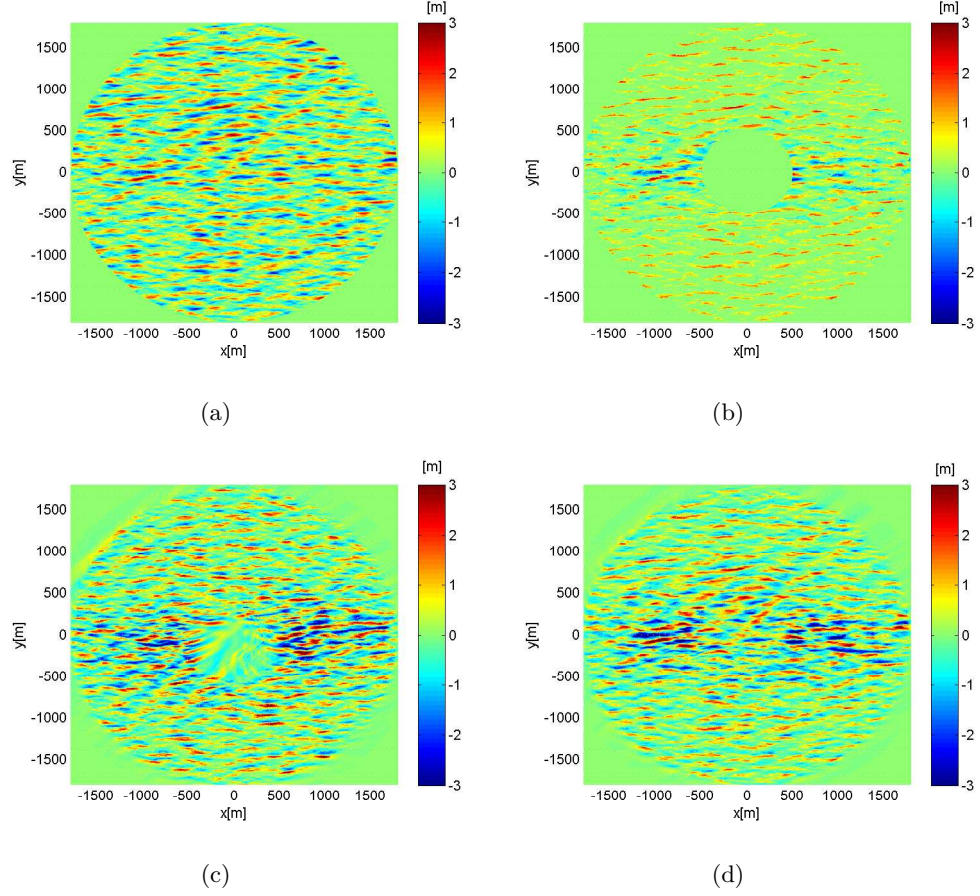


Figure 2: Images of the combined sea WS15 with wind waves from the North and swell from SE. Image (a) shows the real sea, and (b) the shadowed sea at the same instant. Image (c) shows the elevation shortly after the start of the simulation when the waves do not yet fully occupy the blind near radar area; at a later time, image (d) shows that the blind area has been filled with waves through the dynamic averaged evolution scenario.

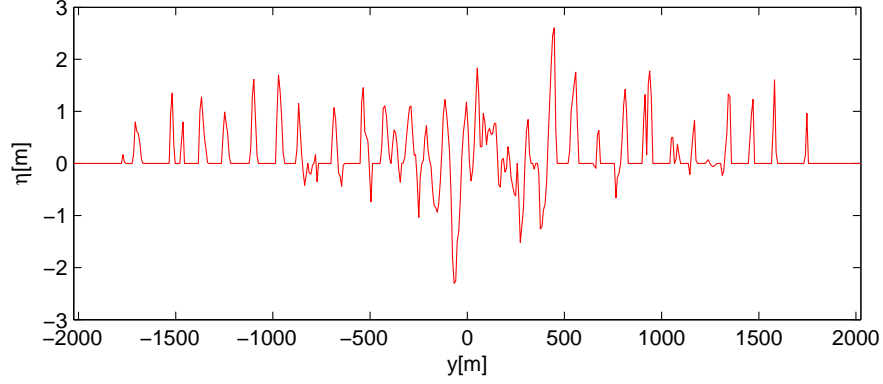


Figure 3: A cross section coinciding with the  $y$ -axis shows the shadowed waves (wind waves from right to left); observe the severe shadowing outside the blind area  $(-500, 500)$ .

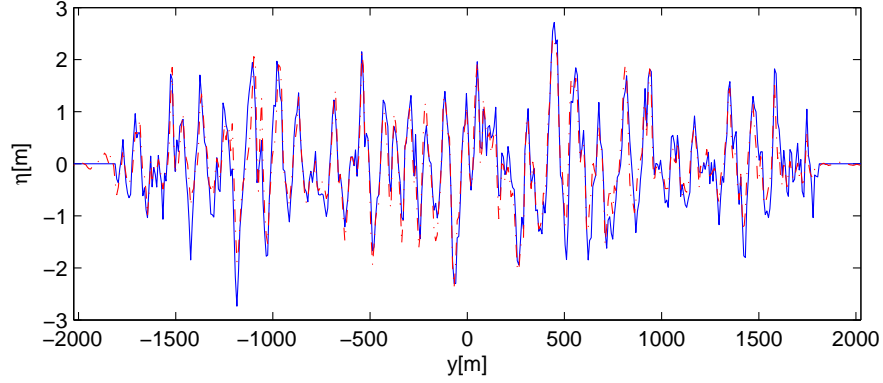


Figure 4: Cross section along  $y$ -axis showing the true elevation (blue, solid) and the reconstructed elevation  $R^1$  (red, dashed).

429 is rather severe: beyond  $r = 500$  hardly any wave troughs are visible. Despite  
 430 this poor quality of the observation, the DAES procedure produces a recon-  
 431 struction of the wave elevation as shown in Figure 4. This figure shows plots  
 432 of the synthesized elevation, referred to as "true wave", and the reconstruction  
 433  $P(t_1; \tau = 0)$  obtained by DAES at a time  $t_1$  such that the simulation has al-  
 434 ready run sufficiently long for the reconstructed waves to fill the entire blind  
 435 zone. Observe that the reconstruction is better near the radar, near  $y = 0$ ,  
 436 than for larger distances from the radar where the dynamic averaging cannot

437 yet sufficiently improve the poor quality of the observation data near the edge  
 438 of the domain.  
 439 Figure 5 shows time traces of the  $R^1$ -reconstructed elevation and the true ele-  
 440 vation at the radar position for WS15. The entrance effect at early times when  
 441 the wind-waves and swell have not yet completely arrived at the radar position  
 442 is clearly visible. This figure indicates that the entrance effect is visible until  
 443 approximately 80 s, which is close to the time that is needed for the most en-  
 444 ergetic wind waves to travel with group speed 7.4 m/s from the inner ring of  
 radius 500 m to the radar.

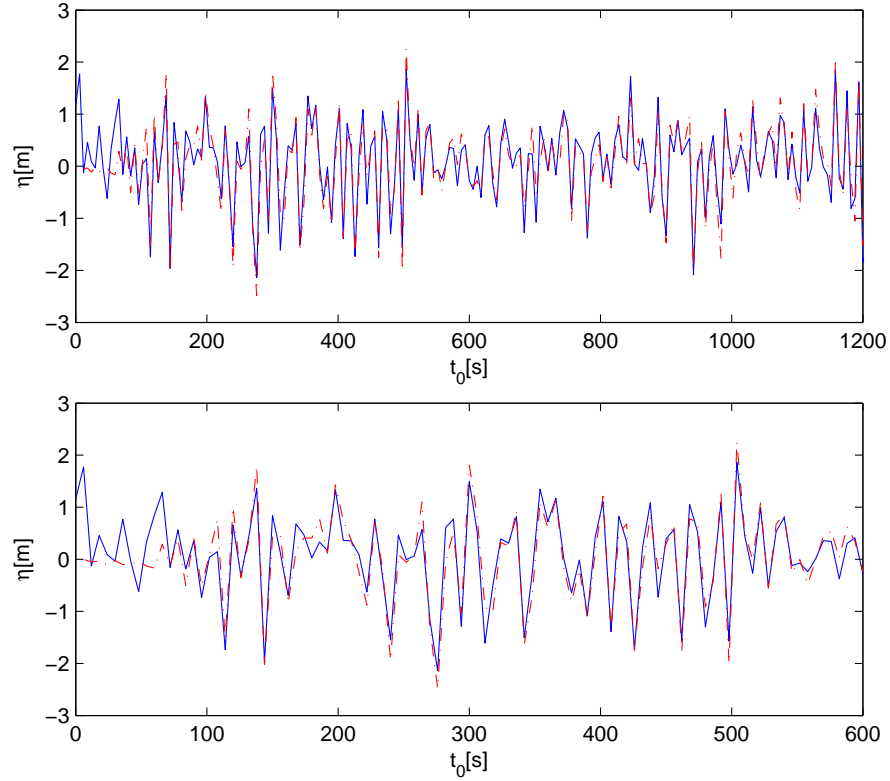


Figure 5: Time traces of elevation at the radar position for case WS15. In blue (solid) the true elevation, in red (dashed) the reconstruction  $R^1$  that started at time 0. The enlarged lower plot from 0 to 300 s shows the entrance effect that only after some 80 s the faster and slower waves reached the radar position to obtain sufficient accuracy.

445

446 *4.2.2. Correlation as measure for accuracy*

447 The accuracy of the reconstruction and prediction is quantified by the cor-  
 448 relation coefficient  $Corr$ , which correlates the wave elevation at one instant ob-  
 449 tained from the simulation ('simul') with the synthetic wave elevation ('data')  
 450 at the same instant according to

$$Corr(data, simul) = \frac{\langle data, simul \rangle}{|data| |simul|} \quad (15)$$

451 Here  $\langle, \rangle$  denotes the inner product over space  $\mathbf{x}$ . Note that  $Corr$  defined in  
 452 this way is related to the normalized point square error according to

$$\frac{|data - simul|^2}{|data| |simul|} = \frac{|data|^2}{|simul|^2} + \frac{|simul|^2}{|data|^2} - 2Corr(data, simul) \quad (16)$$

453 In particular when 'data' and 'simul' have the same norm, it holds

$$\frac{|data - simul|^2}{|data|^2} = 2(1 - Corr(data, simul)) \quad (17)$$

454 The correlation will also be used to quantify the quality of future predictions.  
 455 Using the notation  $P(t_0, \tau)$  introduced in equation (14) for the predicted wave  
 456 elevation starting with the reconstruction at time  $t_0$  a time  $\tau$  ahead, and de-  
 457 noting by  $\eta(t_0 + \tau)$  the synthetic wave elevation from equation (2), their spatial  
 458 correlation will be denoted by

$$c(t_0, \tau) = Corr(P(t_0, \tau), \eta(t_0 + \tau)). \quad (18)$$

Then in order to obtain a statistically more reliable average correlation coefficient  $corr$ , the average is taken over an interval of  $t_0$  values:

$$corr(\tau) = \frac{1}{J} \sum_{j=1}^J c(t_{0j}, \tau) \quad (19)$$

To avoid entrance effects, the computation of  $corr(\tau)$  is restricted to times  $t_0$  such that all waves have evolved to fill completely the blind zone. For the presented simulations, this distance (of 1000 m) is covered by the wind waves with group speed at peak frequency in approximately 136 s, i.e.  $68dt$ ; for the swell waves with double group speed, this time is 68 s. The number of simulation steps  $J$  used for calculation of  $corr(\tau)$  has been at least 200 for all presented results.

#### 4.2.3. Accuracy of reconstruction

The correlation has been computed for both sea states W15 and WS15, for various sizes of the spatial domain:  $corr$  is determined for  $r < 50$ ,  $r < 500$  and  $r > 500$ . Results are presented in Tables 2 and 3 for the 'reconstruction', i.e.  $\tau = 0$ ; prediction results for which  $\tau > 0$  will be presented in the next paragraph.

The first column in Tables 2 and 3 indicates the type of input data used in the DAES procedure. 'Sea' refers to the perfect (not shadowed) synthetic waves as input images, but with vanishing elevation in the near radar area  $r < 500$ . In this column  $R^0$  refers to simulations with shadowed waves without applying any reconstruction of the individual images, while  $R^1$  and  $R^2$  refer to the two reconstruction methods as defined in subsection 3.1.

The columns with 'Raw' and 'Rec' show the correlation of the geometric images and the individually reconstructed images with the true wave elevation respectively; the area over which the correlation is taken is the outer ring area



$500 < r < 1800$ .

Table 2: Correlation for W15 averaged over time for various reconstruction methods.

	Raw	Rec	$r < 50$	$r < 500$	$r > 500$
Sea	1.00	1.00	0.99	0.99	1.00
$R^0$	0.71	0.71	0.82	0.87	0.83
$R^1$	0.71	0.75	0.95	0.95	0.89
$R^2$	0.71	0.75	0.89	0.91	0.84

483

Table 3: Same as 2 now for bi-modal sea state WS15.

	Raw	Rec	$r < 50$	$r < 500$	$r > 500$
Sea	1.00	1.00	0.99	0.99	1.00
$R^0$	0.70	0.70	0.85	0.88	0.83
$R^1$	0.70	0.74	0.95	0.95	0.89
$R^2$	0.70	0.73	0.89	0.90	0.83

484 As illustration, for a typical case, the correlation between the true sea and  
485 the  $R^1$ -reconstruction in the radar area ( $r < 50$  m and  $r < 200$  m) is given in  
486 Figure 6 as function of increasing time during the DAES process. The entrance  
487 effect is clearly visible just as in Figure 5; the waves need approximately 160 s  
488 to fill up the near-radar area of radius 200 m.

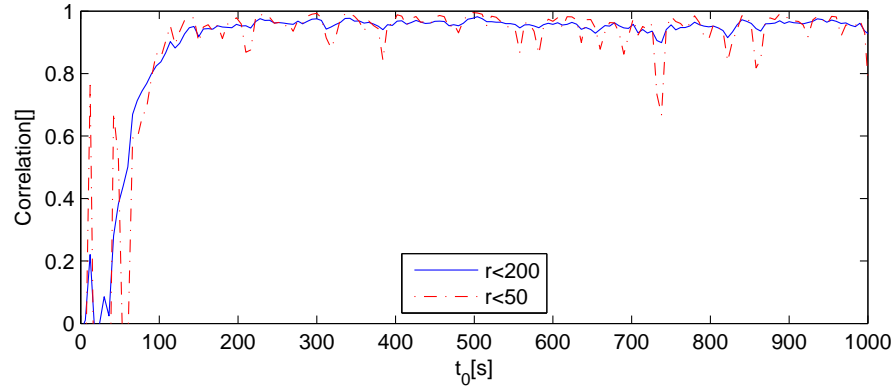


Figure 6: Correlation between true sea and the  $R^1$ -reconstruction for case WS15 in the radar area with radius 200 m (blue) and radius 50 m (red) at times after the start of the reconstruction. Observe that after some 160 s the reconstruction has filled these regions and becomes more accurate.

#### 4.2.4. Accuracy of prediction

The eventual aim of the simulation scenario is to predict in future time the elevation in the near-radar area. At each time  $t_0$  during the simulation, the obtained reconstruction at that time  $P(t_0, \tau = 0)$  can be taken as initial state for a prediction according to equation (14), without new updates. In Figure 7 is shown a prediction at the radar position for the sea state WS15 with reconstruction method  $R^1$ . For an initial time  $t_0 > 160$  larger than the filling time of the near-radar area, the predicted wave elevation and the true wave elevation at the radar position are shown as function of prediction time  $\tau$ .

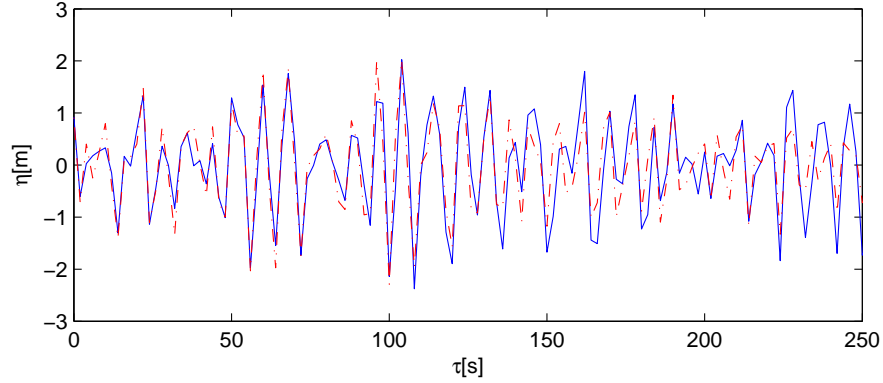


Figure 7: For WS15, the figure shows the prediction (red,dashed) of the elevation compared to the true elevation at the radar position; observe that after 120 s the prediction becomes less accurate.

Figures 8 and 9 show results for prediction based on DAES applied to the true sea (perfect non-shadowed waves) and the  $R^1$ -reconstruction for case W15 and WS15 respectively. As expected, for increasing prediction time the correlation decreases. Prediction of the wind waves W15 can be done for a time horizon of 2.9 minutes with correlation above 0.9, and for 3.6 minutes with correlation above 0.8; for the combined wind-swell waves WS15 these times are 2 minutes and 3.3 minutes respectively. Observe the steeper decrease in the graphs of WS15 after 120 s, which is approximately the travel time of swell waves at

506 peak group velocity; hence after that time, swell waves are not present in the  
 507 prediction anymore.

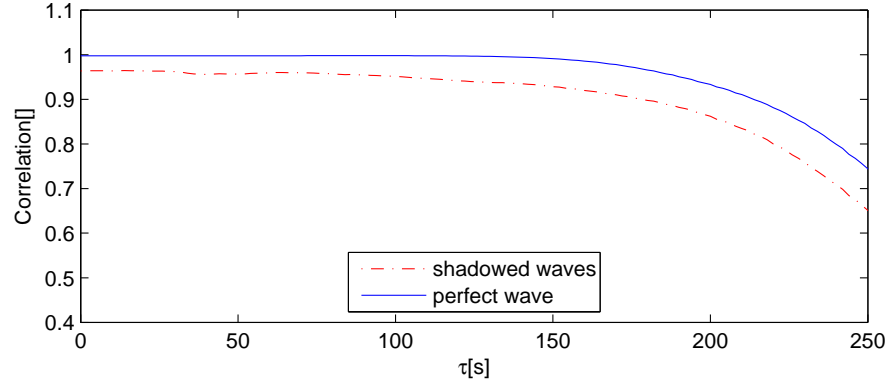


Figure 8: Correlation between predicted and true elevations in a radar area of radius 200 m using as input in the prediction method the true sea (blue, solid) and the shadowed sea of W15 (red, dashed).

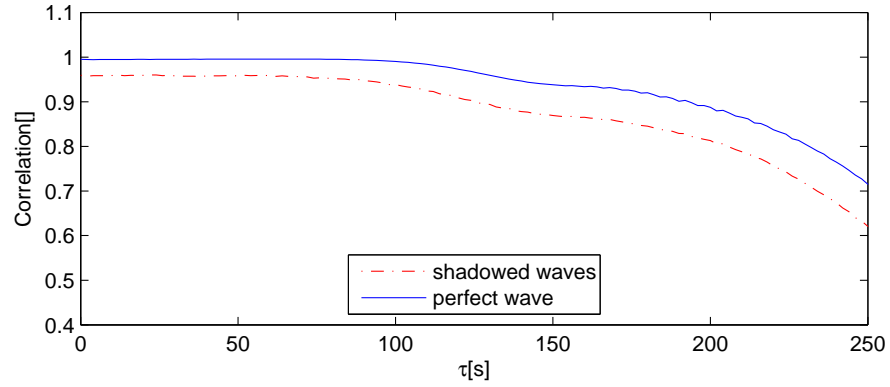


Figure 9: Same as Figure 8 now for WS15.

## 508 5. Discussion of results

### 509 5.1. Reconstruction method

510 The high correlations in Tables 2 and 3 for the case of a perfect 'Sea' (the non-  
 511 shadowed synthetic waves) as input, show that the dynamic averaging procedure

512 and the evolution to fill the near-radar area  $r < 500$  proceeds almost perfectly.  
 513 The tables also show that the reconstruction of each single image only slightly  
 514 improves the correlation, at most 4% for  $R^1$  and  $R^2$ . For all three individual  
 515 reconstructions, the DAES improves the reconstruction substantially, with best  
 516 results for the vertical shifting method  $R^1$ , for which the correlation increases  
 517 from 0.75 in the outer ring to 0.95 in the near-radar area.  
 518 The comparison of the  $R^1$ -reconstructed and true elevation in Figure 6 shows  
 519 that variations of the correlation over the larger disc of radius 200 m are much  
 520 smaller than over the 50 m disc; this may be due to a poor reconstruction of  
 521 relatively small areas in the outer ring  $500 < r < 1800$ .

## 522 5.2. Predictability

523 The results in Figures 8 and 9 show the capabilities and limitations of the  
 524 prediction. The physically maximal prediction time can be roughly estimated  
 525 as the travel time from the outer region towards the radar (1800 m) for the most  
 526 energetic waves at peak frequency. Using the value of the group velocity of the  
 527 wind waves of 7.4 m/s, this leads to a maximal prediction horizon of 240 s for  
 528 study case W15; this seems to be a too high estimation since Figure 8 shows a  
 529 rather low correlation of 0.7 at that time for the best possible prediction with  
 530 the true sea.

531 On the other hand, for the combined wind-swell sea, a similar reasoning based  
 532 on the speed of swell waves is too pessimistic for the study case WS15: the  
 533 correlation of prediction with the true sea is around 0.9 at that time. This can be  
 534 explained by the fact that in the study case the swell waves have approximately  
 535 10% of the energy of the wind waves, which causes that the wind waves dominate  
 536 the correlation, which is only slightly less than for W15 until 250 s, despite the  
 537 fact that the effects of swell are actually absent after 120 s. The swell effect can  
 538 also be observed by comparing the predicted elevation with the true elevation

at the radar position as depicted in Figure 7; the amplitude prediction becomes less accurate after around 120 s although the phase is still captured quite well for longer times.

### 5.3. *Scaling*

The observation from Figure 7 that the variance of the predicted wave elevation decreases with increasing  $\tau$  is also due to the fact that for values of  $\tau$  further into the future, the waves arriving at the radar location originate from further distances where the shadowing is more severe and the variance of the observation is lower; after sufficiently long time no wave information will be available at all anymore. Using one scaling factor  $\alpha$  based on the variance of the entire observed image and the true variance of the waves as was proposed in equation (6), does not take into account this decreased visibility at large ranges from the radar and in fact does not even guarantee a correct variance at the radar for  $\tau = 0$ . An alternative which is supposed to be practical and feasible for real life applications is proposed by Naaijen and Wijaya (2014): a time history of the wave elevation at the radar position (e.g. by an auxiliary wave buoy or via recorded ship motions) and a time history of the predicted wave elevation can be recorded and used to calculate the variance of the true waves and the prediction. By taking the ratio of these variances, a scaling factor dedicated for the radar location can be obtained. Such a scaling factor can also be computed as a function of  $\tau$ , thus removing the aforementioned effect of decreasing variance of the prediction with increasing  $\tau$ .

### 5.4. *MED and bimodal sea state*

In subsection 3.2 it was explained how the wave components obtained from a 2D FFT are propagated in the main evolution direction (MED). In case of multi-modal sea states, it depends on the difference between the propagation

565 directions of the various modes how much of the total wave energy represented  
 566 by the obtained components is propagated in the correct direction. The sea state  
 567 WS15 was designed in such a way that the amount of energy represented by  
 568 wave components propagating in opposite directions relative to the total wave  
 569 energy is very limited which may explain the small differences in the obtained  
 570 accuracy between W15 and the multi-modal case WS15. Multi-modal seas with  
 571 substantial counter propagating waves require an evolution method that takes  
 572 into account a splitting of waves in two opposite directions. Information from  
 573 the directional spectrum can be used for this splitting, see Atanassov et al.  
 574 (1985).

#### 575 *5.5. Parameter dependence and robustness*

576 It has been remarked already that the dimensionless quantity in the vertical  
 577 direction that determines the effects of shadowing is the ratio of radar height  
 578 and significant wave height: the larger this ratio, the less effect of shadowing  
 579 at a fixed position. This has been confirmed for other study cases that will  
 580 not be reported here. The dimensionless quantity in the horizontal direction is  
 581 the ratio of distance to the radar and the peak wave length, and has the same  
 582 consequence. The length of the maximal prediction interval in case of multi-  
 583 modal sea states will depend in a somewhat complicated way on the relative  
 584 energy contents and the difference of group speed of the wind waves and swell.  
 585 For the study case described above (with 3 times larger significant wave height  
 586 for the wind and with 2 times faster speed of the swell) the correlation as  
 587 measure of quality seems to be too crude to identify the full effect of the swell;  
 588 yet in observations of the spatial plots (or on cross sections) the difference can  
 589 be noticed somewhat.

590 As is already indicated in Tables 2 and 3, almost irrespective the reconstruction  
 591 of the shadowed seas, the DAES process produces substantially improved results

592 in the near-radar area, with correlations between 0.88 and 0.95 depending on the  
 593 reconstruction method. This robustness of the dynamic averaging and evolution  
 594 scenario was also observed in other simulations. As an example, one other study  
 595 case considered much wider spreading in the wind waves and swell. Although  
 596 given by the same parameters as reported here, the argument  $\theta - \theta_{main}$  in  
 597 the spreading function was divided by 2 (which is sometimes also used). As  
 598 a consequence, there is more overlap between the two sea states, and hence  
 599 more counter propagating waves that will be evolved in the wrong direction.  
 600 Nevertheless, correlations above 0.9 were obtained in the near radar area. A  
 601 possible explanation for this seemingly inconsistent observation is that the much  
 602 shorter waves cause less shadowing which may be a compensation in the measure  
 603 given by the correlation.

## 604 6. Conclusions and remarks

605 In this paper we introduced a relatively simple and efficient simulation sce-  
 606 nario to transform sequences of synthetic X-band radar images of multi-modal  
 607 sea states into future sea states. The scenario turned out to be rather robust  
 608 and produces reconstruction of the surface elevation in the blind area with cor-  
 609 relation above 0.90 for the case of wind and wind-swell seas, for a ratio of radar  
 610 height and significant wave height of 5. Additional simulations show that the  
 611 correlation improves somewhat for higher values of this ratio because the effect  
 612 of shadowing becomes less. No substantial differences are obtained for seas con-  
 613 sisting of uni-modal wind waves or for multi-modal wind-swell seas.

614 The actual computation time for the simulation with the assimilation can run  
 615 in real time; the required Fourier transforms for the averaging and evolution  
 616 are executed within fractions of real time. For nonlinear simulations this may  
 617 be somewhat longer but will not jeopardize the possibility to run the dynamic

618 averaging-evolution scenario in real time.  
 619 The dynamic averaging-evolution scenario providing updates for a running evo-  
 620 lution can be used in other cases also when a dynamic system experiences pertur-  
 621 bations. We close with mentioning some topics worth of further investigations  
 622 and possible improvements.  
 623 The simplification to consider linear seas above constant depth in this paper  
 624 is mainly for ease of presentation and execution of the scenario; nonlinear seas  
 625 above topography could be dealt with straightforwardly. Apart from this, our  
 626 understanding of waves in real seas still seems to be quite rudimentary. Even  
 627 for linear waves, concepts as the main evolution direction introduced here have  
 628 not yet been related to energy propagation direction; the MED for WS15 is  
 629 remarkably different from the direction of the main energy carrying wind waves  
 630 that determines the direction of the change of the wave profiles during evolu-  
 631 tion. Besides that, detailed studies of nonlinear seas may show phenomena that  
 632 are not captured by linear seas, such as the occurrence and physical processes  
 633 that lead to freak-like waves. If coherent interference is the main process for  
 634 the appearance of long crested freak waves with relatively low Benjamin-Feir  
 635 index, as indicated by Slunyaev et al. (2005), Gemmrich and Garrett (2008) and  
 636 Latifah and van Groesen (2012), the same process may also lead to freak waves  
 637 in short crested waves, enhanced by nonlinear interaction processes.  
 638 In the reconstruction process in this paper, we assumed the significant wave  
 639 height of the sea to be given. Recent investigations showed that this informa-  
 640 tion can actually also be extracted from the geometric images, see Wijaya and  
 641 van Groesen (2015).  
 642 Practical applicability requires the application of the full simulation scenario  
 643 to real radar images and to test the results against accurate measurements.  
 644 Another item to be clarified is if the accuracy of the predicted sea in the inner-



645 radar area as achieved here, is sufficiently high to obtain accurately the forces  
646 on the ship carrying the radar, a topic of direct relevance for various practical  
647 applications. Finally, perturbations from heavy wind bursts may influence the  
648 results; it would be interesting and relevant to investigate the effects.

## 649 **Acknowledgments**

650 We appreciate very much the discussions and suggestions during meetings  
651 with the members of the participating groups in the Industrial Research Project  
652 PROMISED, executed together with MARIN, OceanWaves GMBH, Allseas,  
653 Heerema Marine Contractors and IHC Merwede, with financial support of the  
654 Dutch Ministry of Economical Affairs, Agentschap NL.

655 Alpers, W.R., Ross, D.B., Rufenach, C.L., 1981. On the detectability of ocean  
656 surface waves by real and synthetic aperture radar. *J. Geophys. Res.* 86(C7),  
657 6481-6498.

658 Aragh, S., Nwogu, O., 2008. Variation assimilating of synthetic radar data into a  
659 pseudo-spectral wave model. *J. Coastal Research : Special Issue* 52, 235-244.

660 Atanassov, V., Rosenthal, W., Ziemer, F., 1985. Removal of ambiguity of two-  
661 dimensional power spectra obtained by processing ship radar images of ocean  
662 waves. *J. Geophys. Res.* 90(C1), 10611067.

663 Blondel, E., Naaijen, P., 2012. Reconstruction and prediction of short-crested  
664 seas based on the application of a 3D-FFT on synthetic waves : Part 2-  
665 Prediction. In : *Proceedings of the 31st International Conference on Ocean,*  
666 *Offshore and Arctic Engineering*, Rio de Janeiro, Brazil, pp. 55-70.

667 Borge, J.C.N., Reichert, K., Dittmer, J., 1999. Use of nautical radar as a wave  
668 monitoring instrument. *Coastal Engineering* 37, 331-342.

669 Borge, J.C.N., Rodriguez, G.R., Hessner, K., Gonzalez, P.I., 2004. Inversion of  
670 Marine Radar Images for Surface Wave Analysis. *J. Atmos. Oceanic Technol.*  
671 21, 1291-1300.

672 Buckley, J.R., Aler, J., 1998. Enhancements in the determination of ocean sur-  
673 face wave height from grazing incidence microwave backscatter. In : Proceed-  
674 ings of IEEE IGARS, Seattle, USA, pp. 2487-2489.

675 Clauss, G.F., Kosleck, S., Testa, D., 2012. Critical situations of vessel operations  
676 in short crested seas forecast and decision support system. *J. Offshore Mech.*  
677 *Arct. Eng.* 134(3), 031601.

678 Dankert, H., Rosenthal, W., 2004. Ocean surface determination from X-band  
679 radar image sequence. *J. Geophys. Res.* 109, C04016.

680 Gangeskar, R., 2014. An algorithm for estimation of wave height from shadowing  
681 in X-band radar sea surface images. *IEEE Trans. Geosci. Remote Sens.* 52,  
682 3373-3381.

683 Gemmrich, J., Garrett, C., 2008. Unexpected Waves. *J. Phys. Oceanogr.* 38,  
684 2330-2336.

685 Goda, Y., 2010. *Random Seas and Design of Maritime Structures*, 3rd edition,  
686 World Scientific, Singapore.

687 Jefferys, E., 1987. Directional seas should be ergodic. *Appl. Ocean Res.* 9, 186-  
688 191.

689 Latifah, A.L., Van Groesen, E., 2012. Coherence and predictability of extreme  
690 events in irregular waves. *Nonlin. Processes Geophys.* 19, 199-213.

691 Naaijen, P., Blondel, E., 2012. Reconstruction and prediction of short-crested  
692 seas based on the application of a 3D-FFT on synthetic waves : Part 1-

693 Reconstruction. In : Proceedings of the 31st International Conference on  
694 Ocean, Offshore and Arctic Engineering, Rio de Janeiro, Brazil, pp. 43-53.

695 Naaijen, P., Wijaya, A.P., 2014. Phase resolved wave prediction from synthetic  
696 radar images. In : Proceedings of 33rd International Conference on Ocean,  
697 Offshore and Arctic Engineering OMAE, ASME, San Fransisco, USA.

698 Naaijen, P., Trulsen, K., Blondel, E., to be published. Limits to the extent of  
699 the spatio-temporal domain for deterministic wave prediction.

700 Plant, W.J., Farquharson, G., 2012a. Wave shadowing and modulation of mi-  
701 crowave backscatter from the ocean. J. Geophys. Res. 117, C08010.

702 Plant, W.J., Farquharson, G., 2012b. Origins of features in wave number-  
703 frequency spectra of space-time images of the ocean. J. Geophys. Res. 117,  
704 C06015.

705 Slunyaev, A., Pelinovsky, E., Soares, C.G., 2005. Modeling freak waves from the  
706 North Sea. Appl. Ocean Res. 27, 12-22.

707 Wijaya, A.P., Van Groesen, E., to be published. Determination of the significant  
708 wave height from shadowing in synthetic radar images.

709 Wu, G., 2004. Direct Simulation and Deterministic Prediction of Large-scale  
710 Nonlinear Ocean Wave field. Ph.D. thesis. Massachusetts Institute of Tech-  
711 nology.

712 Young, I.R., Rosenthal, W., Ziemer, F., 1985. A three dimensional analysis of  
713 marine radar images for the determination of ocean wave directionality and  
714 surface currents. J. Geophys. Res. 90, 1049-1059.

715 Ziemer, F., Rosenthal, W., 1987. On the Transfer Function of a Shipborne Radar  
716 for Imaging Ocean Waves. In : Proceedings IGARSS'87 Symp., Ann Arbor,  
717 pp. 1559-1564.